Microscopic picture of magnetic correlation with loss of uniaxial anisotropy upon swift ion beam irradiation in an interlayer coupled system

2010 New J. Phys. 12 103003

(http://iopscience.iop.org/1367-2630/12/10/103003)

New Journal of Physics
The open-access journal for physics

Microscopic picture of magnetic correlation with loss of uniaxial anisotropy upon swift ion beam irradiation in an interlayer coupled system

Amitesh Paul[1,3] **and Stefan Mattauch**[2]

[1] Helmholtz-Zentrum Berlin für Materialien und Energie GmbH, Hahn-Meitner-Platz 1, D-14109 Berlin, Germany
[2] Institut für Festkörperforschung IFF-4 'Streumethoden', JCNS, Forschungszentrum Jülich GmbH, D-52425 Jülich, Germany
E-mail: amitesh.paul@helmholtz-berlin.de

New Journal of Physics **12** (2010) 103003 (17pp)
Received 18 May 2010
Published 5 October 2010
Online at http://www.njp.org/
doi:10.1088/1367-2630/12/10/103003

Abstract. Exclusive evidence of magnetic structure modification has been revealed by depth-sensitive polarized neutron scattering measurements in an antiferromagnetically coupled specimen upon swift heavy ion irradiation. The effects are independent of any structural modifications within the system (such as intermixing or roughness) that may normally have contributed to the changes in magnetic structure as well. The modifications include (a) the loss of uniaxial anisotropy, (b) changes in the variation of the mean magnetization angle and (c) changes in the variation of the lateral and longitudinal magnetic correlation lengths. We explain the changes within the thermal spike model. The possibility of controlling local magnetization can be foreseen from these results, which can be done even without damaging the structure.

[3] Author to whom any correspondence should be addressed.

Contents

1. Introduction

The slowing down of a swift heavy ion (velocity comparable to the Bohr velocity of electrons: $1.4 \times 10^9\,\mathrm{cm\,s^{-1}}$) in solids results from an energy loss in solids. This can be caused either by inelastic collisions with electrons (S_e [keV nm^{-1}] is the electronic stopping power) or by elastic collisions with the nuclei of the target atoms (S_n [keV nm^{-1}] is the nuclear stopping power). With the exception of the low energy range, the electronic loss dominates, exceeding the nuclear energy loss by 2–3 orders of magnitude. It can be seen that conventional ion irradiation (energy less than a few MeV) produces an electronic stopping power of a few keV nm^{-1} and therefore ion track damage does not occur and nuclear collisions dominate. High-energy heavy ion irradiations, on the other hand, create crystal damage through inelastic electronic collisions as electronic stopping dominates (leading to microstructural changes, interface modifications and phase transformation as energy is dissipated in the lattice).

Ions with energies of the order of a few keV to a few hundreds of keV generate a sequence of collisions known as a collision cascade (here, all ion energies are expressed as energy/a.m.u.). During this process, energies of the impinging ions displace atoms and electrons of the target material several lattice sites away, resulting in relocations, and this results in interface mixing. Depending upon the mass of the target, two types of ion beam mixing can happen. If the average mass and density of the target are low, the mixing will occur only through ballistic mixing. On the other hand, if the mass and density of the target are high, thermal spike ($\sim 10^{12}$ s) mixing happens. Experimental studies of bilayers by Johnson *et al* [1] and Cheng [2] have shown the influence of thermodynamic parameters on the mixing rate in the low-temperature regime in the case where the spikes are well developed [3]. Alternatively, radiation-enhanced diffusion (RED) can also take place, which is simply an enhancement of normal thermal diffusion by virtue of the ion irradiation process [4].

In the case of a metallic system, it has been observed that damage production can take place only above a certain threshold value of S_e. Metals such as Fe and Co have a certain sensitivity to S_e that varies by around a few tens of keV nm^{-1} [5]. The existence of a threshold in S_e value (for features of damage production) is generally understood in terms of the thermal spike model [6]. A part of the energy from the electronic system gets transferred to the lattice via electron–phonon interactions. This results in a rise in the local temperature along the ion track (labeled as the thermal spike and suitable for metals) crossing the melting temperature of the material. In the case of two different elements, any intermixing is thus primarily dependent upon their heat of mixing (difference between the enthalpy of a mixed specimens and the sum

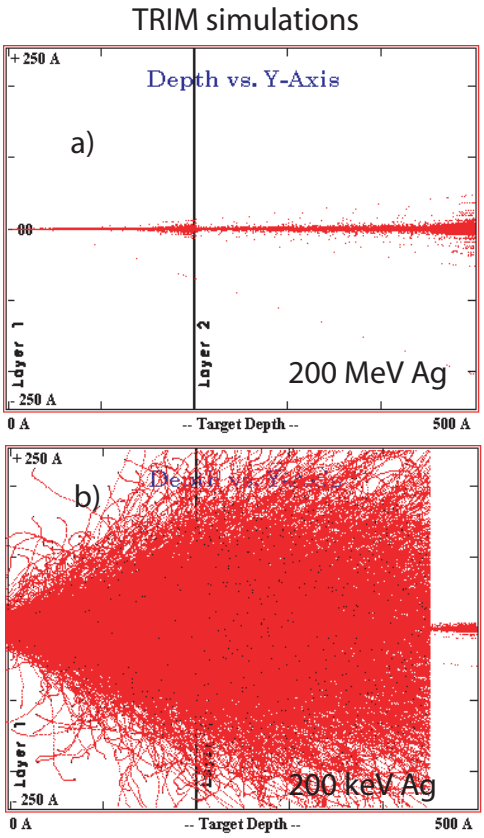

Figure 1. TRIM simulations for 1×10^5 ions on a Co–Cu layer target for a range of 50.0 nm showing the trajectory in the case of (a) 200 MeV and (b) 200 keV energies.

of the enthalpies of its individual specimens at the same pressure and temperature) properties. For example, Co–Cu is characterized by positive heat of mixing and is considered immiscible.

Ion mixing is typical of low-energy ion irradiation effects (typical commercial ion-implantation systems provide ions of energy in the range 40–400 keV). As a recent example, one may look at silicide formation and ion beam mixing of Fe/Si bilayers due to Ar-, Xe- and Au-ion irradiations at room and liquid-nitrogen temperatures [7]. Chapart *et al* [8] showed that the easy magnetization direction of CoPt multilayers can be rotated in-plane upon 30 keV He^+ ion irradiation. Interfacial mixing leads to a reduction in the interface anisotropy. For a complete review of the topic, see [9]. Magnetic domain analysis is relevant to understand the relationship between microstructure and magnetic anisotropy in magnetic materials in the thin film form, particularly when they are interlayer coupled. Low-energy ion irradiation (5 keV He^+) has been quite successful in manipulating interlayer coupling in the Fe/Cr/Fe trilayer [10] or in tailoring exchange coupling at the FeNi/FeMn interface [11].

In our case, however, we eliminate such low-energy effects using a MeV range of ions, which have a very different impact altogether. In the low-energy regime, ballistic mixing causes atomic rearrangements, which subsequently modify magnetic properties. Swift heavy ions, on the other hand, are liable to produce amortization in a perturbed cylinder along the (very straight ion path as compared to keV range of ions) ion path beyond a threshold of energy transfer [12]. Figure 1 shows the impact on the ion trajectory for (a) 200 MeV ions and (b) 200 keV ions for

a Co–Cu layered system. In the case of swift heavy ions, the trajectory is fairly confined within a cylindrical range of a few nanometers, while in the case of a keV range of ions it is rather widely distributed.

Swift heavy ion irradiation experiments have previously been performed on interlayer coupled Fe/Cr (200 MeV Ag^{+}) [13] and Co/Cu MLs (1 MeV Si^{+} ions) [14]. The observation revealed a drastic decrease in the giant magnetoresistance (GMR) (for details, see various contributions in [15]) with increasing fluence in both cases. The drastic changes were primarily due to the formation of asperities on glass substrates, which would have caused such extensive damage [16]. One may note that Fe/Cr is a miscible ML system, whereas Co/Cu is immiscible, and in both cases the changes were drastic.

Thus, one can easily visualize that the effect on magnetic domains—due to ion irradiation—is heavily shrouded either by strong interfacial structural modification (impact of low-energy ions) or by degradation of the substrate extended to the multilayer (impact of high-energy ions). In the current work, we present our experimental report on the effect of swift heavy ions *exclusively* on magnetic domain correlations in a system that does not show any drastic changes in its structural properties. To the best of our knowledge, the effect on magnetism due to ion irradiation has so far never been reported so exclusively.

2. Experimental details

The multilayers prepared are of the following sequence: SiO_2/Co(1.45 nm)/[Cu(1.02 nm)/Co(1.45 nm)]$_{N=20}$. The thickness of the Cu layers corresponds to the first AF coupling maximum [17]. We have given the details of the preparation and characterization of similar structures in [25]. The hysteresis loops are measured by the longitudinal magneto-optical Kerr effect (MOKE). The microstructure and the layer quality are investigated by low angle x-ray reflectivity (XRR) and x-ray diffuse scattering (XDS) measurements [18]–[20]. XRR and XDS measurements are done using a Bruker-axs D8 diffractometer with Cu-K_α radiation, equipped with Göbel mirrors for the incident and reflected beams instead of conventional Soller slits.

We measured both in specular geometry with the angle of incidence θ_i equal to the exit angle θ_f and in off-specular geometry with an offset of $\Delta\omega = 0.13^\circ$ between θ_i and θ_f. Rocking curve measurements show that at an offset of 0.1° the specularly reflected component is almost completely removed. Thus, in a scan with an offset $\Delta\omega = 0.13^\circ$, one measures the diffuse scattering as a function of the component of the momentum transfer vector normal to the sample plane, Q_z. True specular reflectivity is obtained by subtracting the off-specularly reflected intensity from the specular one. Diffuse scattering as a function of the in-plane component of the momentum transfer vector, Q_x, is measured by keeping the scattering angle 2θ fixed and rocking the specimen around $\theta_i = \theta_f$.

Irradiations were performed at room temperature. We have used the 15 MV Pelletron accelerator of the Nuclear Science Centre, New Delhi, for the irradiation with 200 MeV Ag^{15+} ions. Calculations using the TRIM (transport of ions in matter) code (J P Biersack TRIM91) indicate that 200 MeV Ag ions are implanted in the substrate for films with a maximum thickness of 50.0 nm of the total film thickness used in the present experiments, as the implantation depth is $\sim 10\,\mu$m. Figure 2(a) shows the dominance of electronic energy loss over nuclear energy loss for 200 MeV Ag ions in a Co–Cu system calculated by TRIM. Figure 2(b) shows the calculated energy loss for different ions and energies. The S_e values are

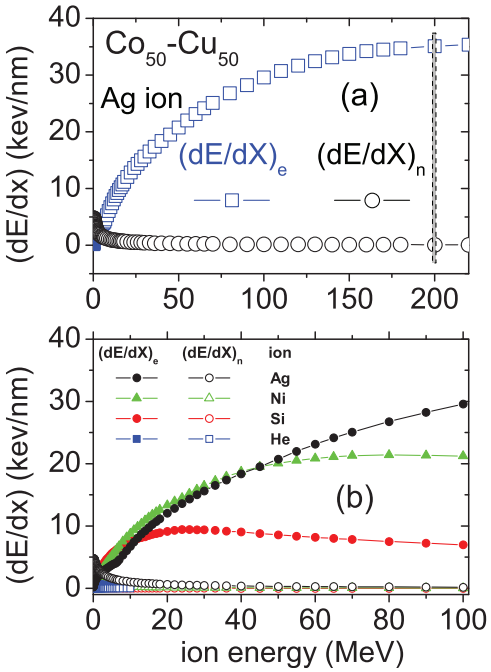

Figure 2. (a) Dominance of electronic energy loss as compared to that of nuclear energy loss for 200 MeV Ag ion irradiation in a Co–Cu system. The dotted line indicates the energy used and thereby the expected range of electronic and nuclear energy losses within the target. (b) The energy loss values in the system depending on various ions with different energies.

well saturated for our choice of 200 MeV Ag ions. For a different ion, either the value would have been much lower or it would have an increasing tendency. The samples were irradiated uniformly for three different fluences of irradiation, 1E12, 3.2E12 and 1E13 ions/cm^{-2}, over an area of $1 \times 1\,\mathrm{cm}^2$ by scanning the ion beam of 1 pnA (particle nano-ampere) current using an electromagnetic scanner at 10^{-6} torr pressure in the chamber.

Polarized neutron reflectivity (PNR) measurements are performed at the polarized neutron reflectometer with the polarization analysis TREFF at the Jülich Center for Neutron Research FRM-2. The neutron wavelength is fixed at $\lambda = 4.73$ Å. The instrument details are described elsewhere [21]. The specimens are kept at room temperature and an external field H_a of up to 1.5 kOe is applied. The direction of H_a is in the plane of the ML and perpendicular to the in-plane uniaxial easy axis of the magnetization determined from magnetization measurements. We perform PNR measurements at five different strengths H_a of the applied field along one branch of the hysteresis loop.

In specular geometry (angle of incidence α_i equal to the exit angle α_f), the reflectivities follow from energy and in-plane momentum conservation laws. Normal wave vector transfers $Q_\perp = \frac{2\pi}{\lambda}[\sin\alpha_i + \sin\alpha_f]$ are probed. Specular reflectivities in the non-spin-flip (NSF) channels (R_{++} and R_{--}) are due to periodicities of the structure and magnetization components collinear to the applied field H_a, whereas reflectivities in the spin-flip (SF) channels (R_{+-} and R_{-+}) are exclusively of magnetic origin and correspond to in-plane magnetization components perpendicular to the guiding field H_a. Off-specular scattering along the in-plane momentum transfer vector $Q_\parallel = \frac{2\pi}{\lambda}[\cos\alpha_f - \cos\alpha_i]$ arises when the in-plane translational symmetry is

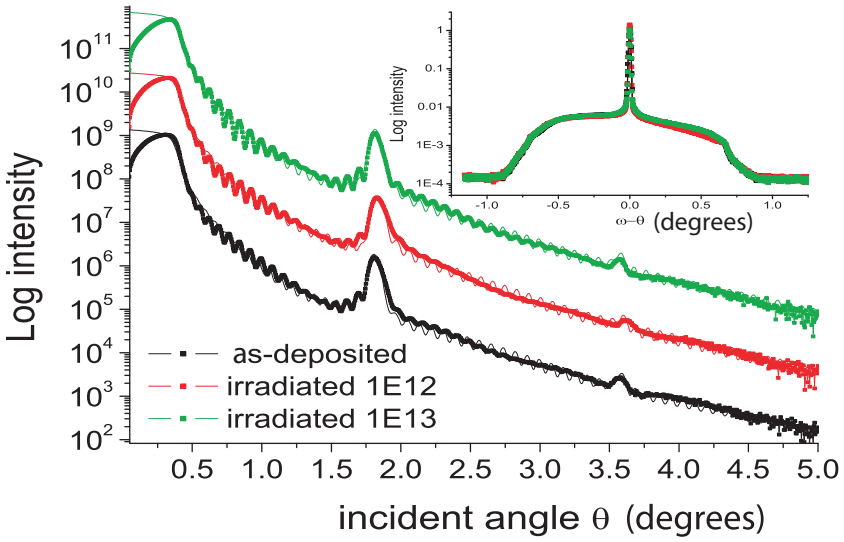

Figure 3. True-specular XRR scans of the ML SiO_2/Co(1.45 nm)/[Cu(1.02 nm)/Co(1.45 nm)]$_{\times 20}$ along with their fits with increasing fluence of irradiation. The curves are vertically shifted for clarity. The inset shows the corresponding XDS spectra.

broken by interface roughness or magnetic domains on a length scale shorter than the in-plane projection of the neutron coherence length $l_{\parallel}$ [22, 23], which is along $Q_{\parallel}$.

3. Experimental results and discussion

3.1. X-ray and magnetooptical Kerr effect (MOKE)

Figure 3 shows the true x-ray specular reflectivity (XRR) as well as the off-specular reflectivity (XDS) from the samples. The Bragg peak due to the periodicity of the ML is clearly visible in the specular reflectivity spectrum at about 1.7°, which agrees very well with the designated periodicity. The true-specular patterns are fitted by the least-square method using the standard optical formalism according to Nevot and Croce [24], as has also been described earlier [25]. We have not considered an interdiffused Co–Cu layer as negligible intermixing is expected for two elements (Co and Cu) with a positive heat of mixing. The thickness of the individual Co and Cu layers and the average $\sigma\,(= 0.6\,\text{nm})$ in each of the ML are determined from these fits. Note that the fits reveal no significant differences in the respective parameters, such as interface roughness or in-plane ($\xi \approx 50\,\text{nm}$) or out-of-plane (greater than the total ML thickness) structural roughness correlations with increasing ion fluence. If the multilayers go from an originally mixed state (e.g. a non-miscible Ag/Fe system [26] irradiated with up to 600 keV Xe) to a de-mixed state, they would easily be detected by XRR as we compare the irradiated profile with that of the as-deposited one. Thus, we may rule out such a possibility. Again, as mentioned before, the ion energy was in keV as compared to our MeV range. We have also checked the variation in width of the Bragg peak from the XRR spectra for different fluences of irradiation and they are found to be well within the error of estimation. Thus the periodicity distribution remains similar and this is also consistent with the neutron measurements reported in a later section. The inset of figure 3 shows the XDS patterns of the specimens with increasing fluence of irradiation.

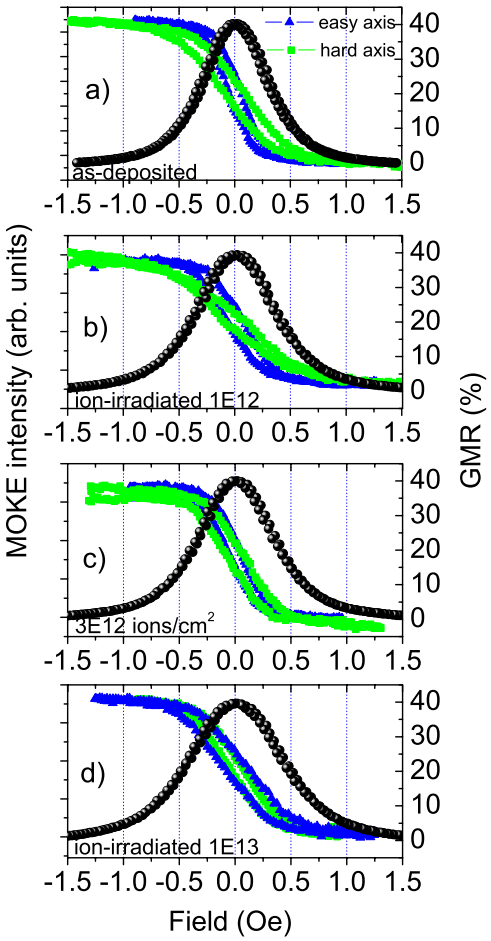

Figure 4. MOKE hysteresis loops for the ML SiO_2/Co(1.45 nm)/[Cu(1.02 nm)/Co(1.45 nm)]$_{\times 20}$ when it is (a) as-deposited and (a–d) ion beam irradiated with a fluence of (b) 1E12 ions cm^{-2}, (c) 3E12 ions cm^{-2} and (d) 1E13 ions cm^{-2}.

In figure 4, we show the magnetization behavior as measured by MOKE. The samples exhibit an in-plane uniaxial magnetic anisotropy. Small differences in the shape of the magnetization loops measured parallel (blue) and perpendicular (green) to the easy axis in the as-deposited case can be seen from the irradiated specimens. These small differences can be seen to be gradually diminishing as we increase the fluence of ion irradiation. This indicates that the growth-induced anisotropy that was intrinsic to the sample is readily destroyed by the fluence of irradiation. Such an anisotropy is induced in the system during growth (the magnetic field used to confine the plasma in a magnetron sputtering unit is usually the most probable reason behind it). Figure 5 shows the difference in anisotropy energies (from the area subtended by the curves parallel and perpendicular to the easy axis) versus the fluence of irradiation from the MOKE curves, indicating loss of anisotropy.

The GMR [27] ratio, however, does not show measurable differences from its value at 40% with changing fluence, measured either along the easy axis or perpendicular to it. The ratio of the magnetic remanence M_r to the magnetic saturation M_s is often used to quantify the fraction

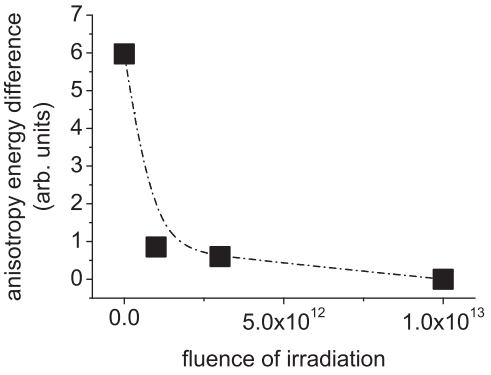

Figure 5. Plot of the difference in anisotropy energies versus fluence of irradiation from the MOKE curves, indicating loss of anisotropy.

of an ML with antiparallel alignment of adjacent film magnetizations at zero external field. This so-called antiferromagnetic coupling fraction (AFF) is given by $\mathrm{AFF} = 1 - M_\mathrm{r}/M_\mathrm{s}$ [28]. The GMR ratio of an ML scales with AFF because only AF coupled regions of a sample can contribute to the magnetoresistance. In all of our samples the AFF fraction lies around 0.42, corroborated with their similar GMR ratio. The ratio of GMR to $M_\mathrm{r}/M_\mathrm{s}$ also remains very much similar, indicative of only bilinear coupling between the layer magnetization and no biquadratic coupling [17].

3.2. Neutron scattering

3.2.1. Specular scattering. Figures 6 and 7 show the specular NSF and SF intensities as a function of incident angle α_i for the as-deposited and ion-beam-irradiated (1E13 ions cm^{-2}) specimens. The intensities around the first order Bragg peak ($Q \approx 0.265$ Å^{-1}) are due to the chemical and magnetic periodicity of the ML. The $\frac{1}{2}$-order Bragg peak ($Q \approx 0.14$ Å^{-1}) due to the antiparallel alignment of Co layers is visible in both SF and NSF channels and for all fields except for the highest field of 1.5 kOe. One may note that the $\frac{1}{2}$-order Bragg intensities in the SF channels are more intense than those in the NSF channels. Although all four channels are fitted within the single-domain approximation, the widths of the $\frac{1}{2}$-order Bragg peak of the SF intensities could not be reproduced because these peaks are diffuse in nature. The presence of this broad $\frac{1}{2}$-order Bragg peak reflects magnetic inhomogeneities along the sample plane on a length scale smaller than $l_\parallel$, which are also vertically correlated.

We fit the specular NSF reflectivities (e.g. open symbols) using the procedures described in [29]: we consider deviations from the purely collinear single-domain configuration by taking into account the non-ideal polarization efficiencies of the neutron optical parts, such as the polarizer and the analyzer. The Co layers ($n = 1, \ldots, 20$) are described by their mean magnetization amplitude $\langle M_n \rangle$ and their angular deviation from the easy axis $-x$, which we describe by ϕ_n and $\phi_{(n+1)}$. We describe $\phi_\mathrm{B} = \phi_n - \phi_{n+1}$. In remanence, the AF coupling forces the magnetizations of adjacent Co layers to collinear, antiparallel alignment. As we increase the field applied in the $-y$-direction, all (n) and $(n+1)$ layer magnetizations rotate symmetrically towards the field. In saturation, $\phi_\mathrm{B} = 0^\circ$. The fitted $\langle M_n \rangle$ values do not show significant variations.

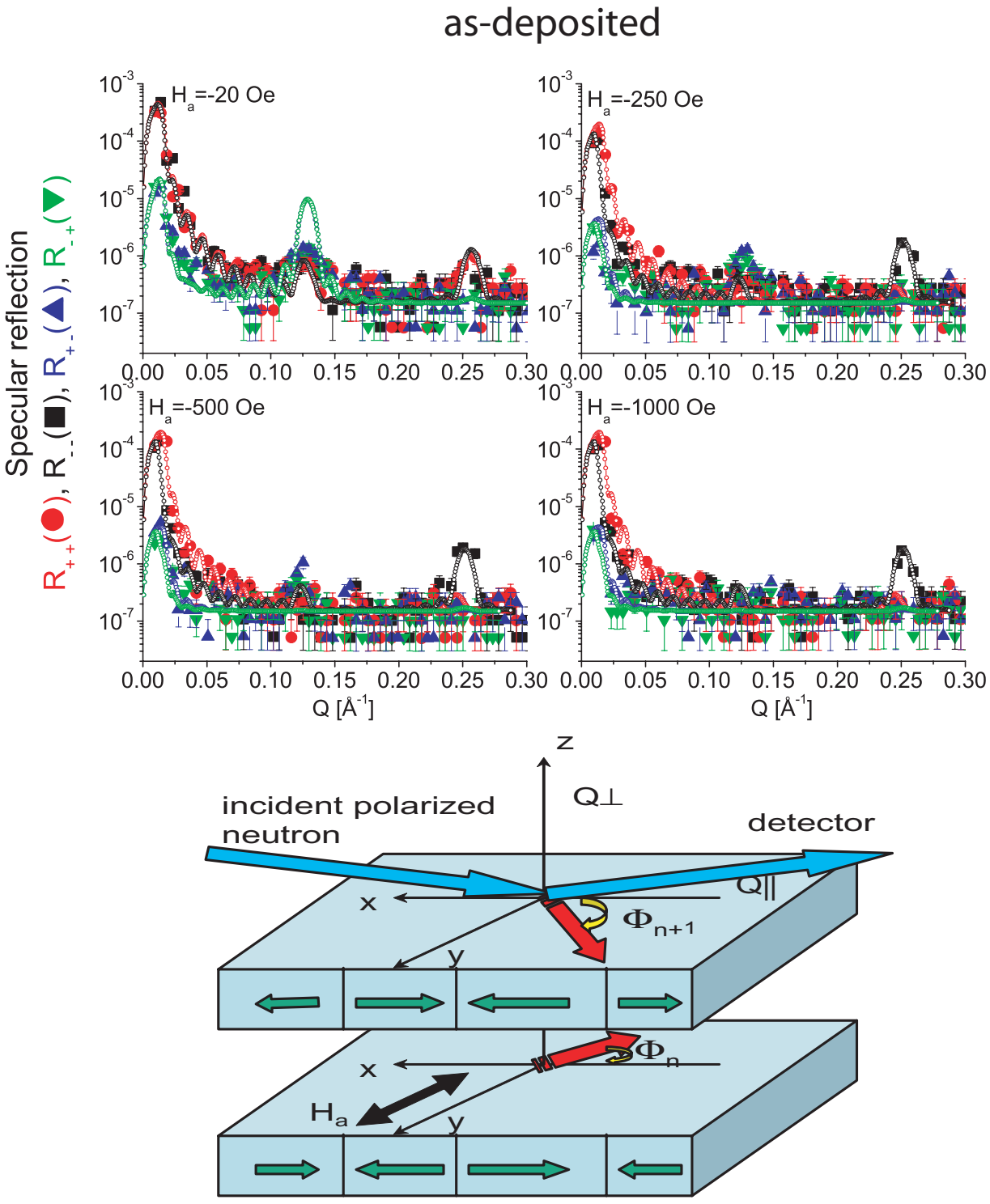

Figure 6. Measured NSF [R_{++} (blue circle) and R_{--} (black square)] and SF [R_{+-} (red triangle) and R_{-+} (green downtriangle)] reflectivity curves of an as-deposited SiO_2/Co(1.45 nm)/[Cu(1.02 nm)/Co(1.45 nm)]$_{N=20}$ ML at different applied fields H_a as indicated. The open symbols in the left panels represent fitted curves for all four channels of polarization. A schematic diagram of the neutron scattering geometry is shown alongside.

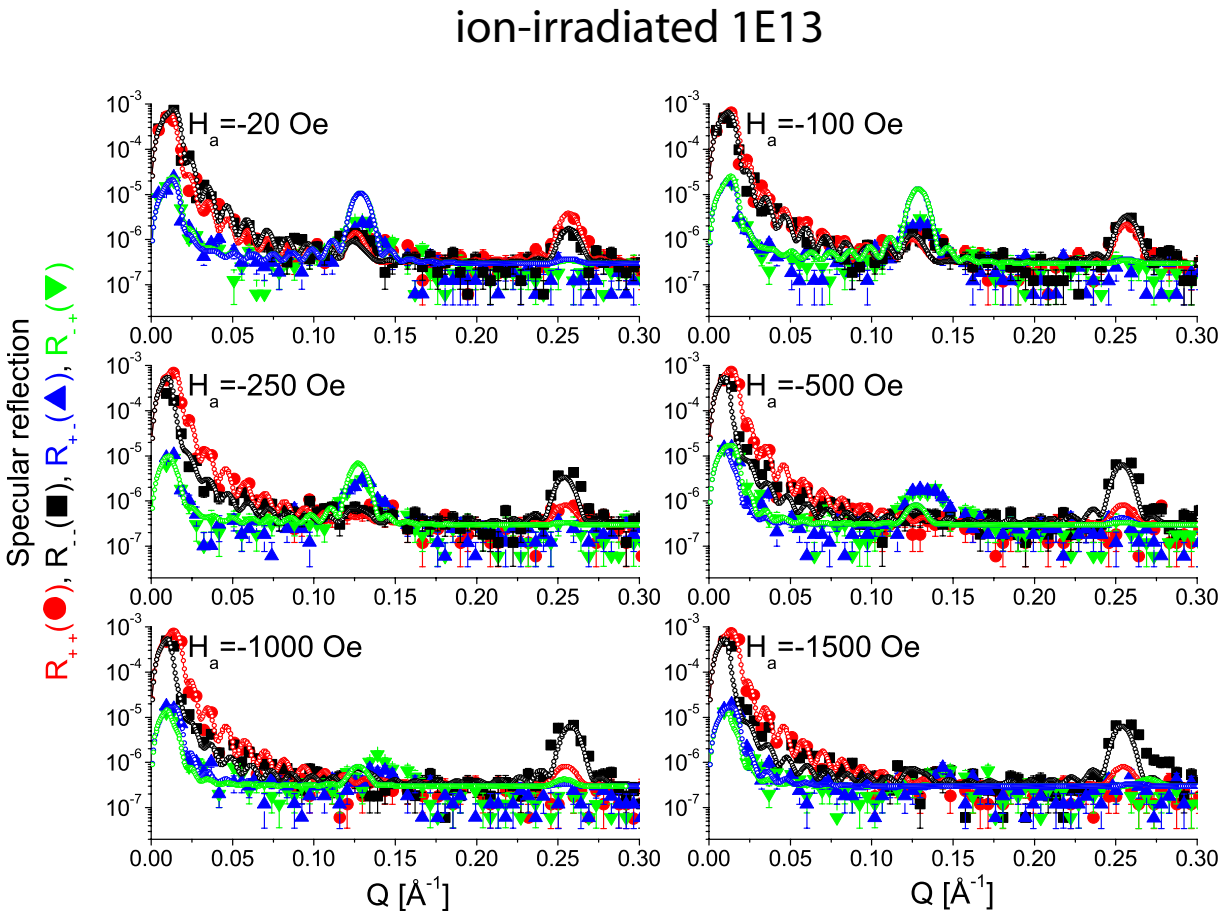

Figure 7. Measured NSF [R_{++} (blue circle) and R_{--} (black square)] and SF [R_{+-} (red triangle) and R_{-+} (green downtriangle)] reflectivity curves of an ion-beam-irradiated (1E13 ions cm^{-2}) SiO_2/Co(1.45 nm)/[Cu(1.02 nm)/Co(1.45 nm)]$_{N=20}$ ML at different applied fields H_a as indicated. The open symbols in the left panels represent the fitted curves for all four channels of polarization.

3.2.2. Off-specular scattering. Diffuse scattering indicates the presence of lateral inhomogeneities caused by domains that are seen in the SF intensity maps shown in figure 8 for different H_a corresponding to the as-deposited and ion-beam irradiated (1E13 ions cm^{-2}) specimens. The $\frac{1}{2}$-order Bragg peak at $Q \approx 0.14$ Å^{-1} is broad along $Q_\parallel$ as well as along $Q_\perp$. Its intensity rapidly shrinks with distance from the specular line and also decreases with increasing H_a. We estimate the lateral size ξ of the vertically correlated domains by simulations of the intensity maps under the distorted-wave Born approximation (DWBA) [22]. We use the fitted values of the angles ϕ_n and ϕ_{n+1} as determined from NSF reflectivities and consider for the simulations a Gaussian fluctuation of these angles, which is denoted as $\langle \Delta\phi_n \rangle$. It is estimated to be approximately $\pm 30^\circ$ for all fields and describes the fluctuation of the angle from domain to domain. These fluctuations are the origin of the enhanced intensities around the $\frac{1}{2}$-order peak in the SF and NSF channels. The simulations are done simultaneously for the NSF and SF specular and off-specular intensities.

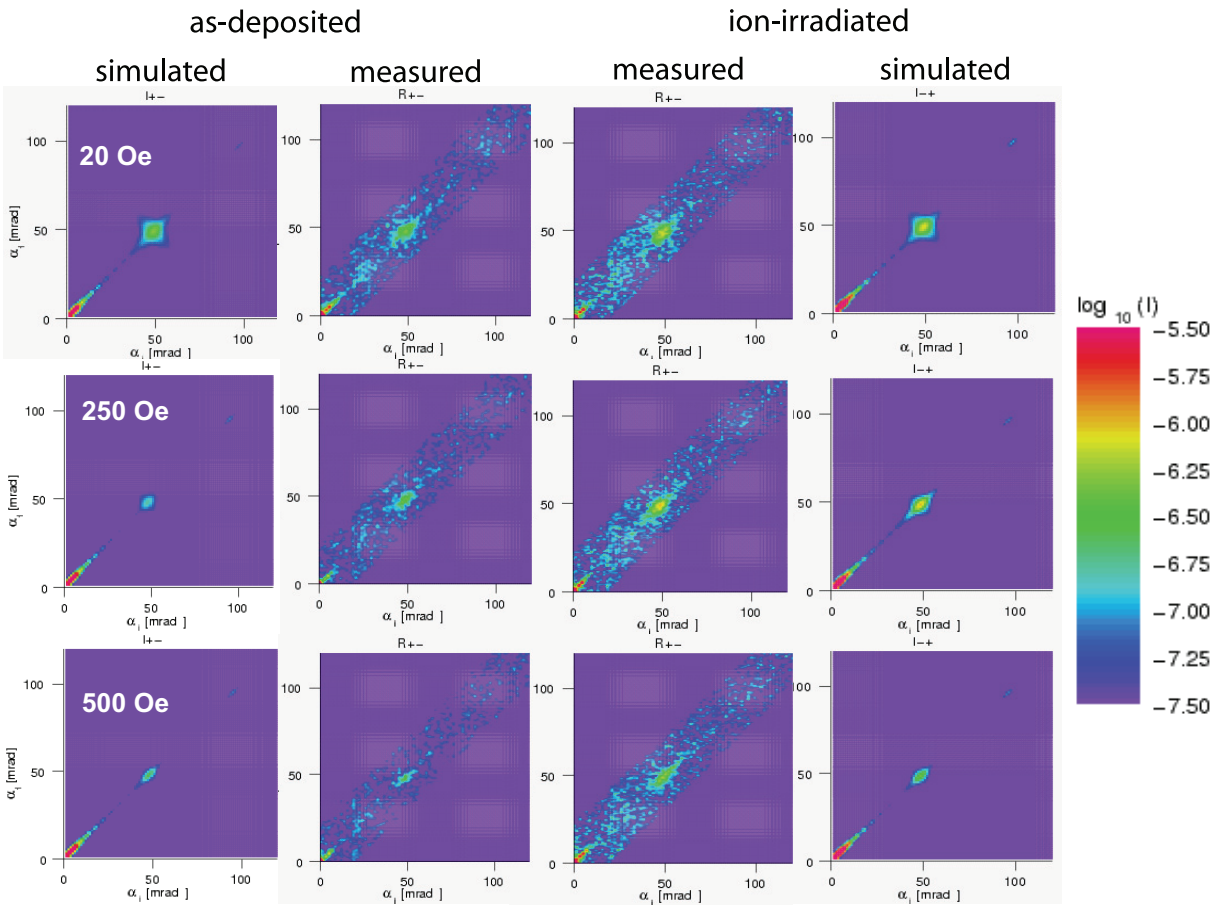

Figure 8. Measured (middle panels) and simulated (side panels) SF intensity maps (I_{-+}) of as-deposited and ion-beam-irradiated (1E13 ions cm^{-2}) SiO_2/Co(1.45 nm)/[Cu(1.02 nm)/Co(1.45 nm)]$_{N=20}$ ML at different applied fields H_a as indicated.

3.2.3. Angular variation of magnetization. Figure 9(a) shows the angular variation in the layer magnetization (ϕ_B) with applied field. One can see already around 500 Oe large magnetization components with parallel alignment ($\phi \approx 80^\circ$), indicating apparent saturation for the as-deposited specimen. At lower fields, the variation is quite different in the case of the ion-beam-irradiated specimen as compared to the as-deposited one. For the as-deposited sample, ϕ_B is typically about 180°. But for the ion-irradiated specimen at highest fluence, the turn angle is about 240°. The turn angle also refuses to go to 0° before the applied field reaches 1.0 kOe. This obviously indicates a stronger coupling strength. However, no such indication could have been drawn from the magnetization curves. This is probably due to the fact that MOKE has a certain depth limitation (∼20 nm), which is equivalent to an 8 bilayer thickness. Thus the information from the lower layers is obscured. GMR measurements, which are depth averaged, also do not reflect such an increase in coupling strength, primarily due to the fact that macroscopic averaging over the whole sample area (1×1 cm^2) may not be sensitive enough to dig out such a small fraction.

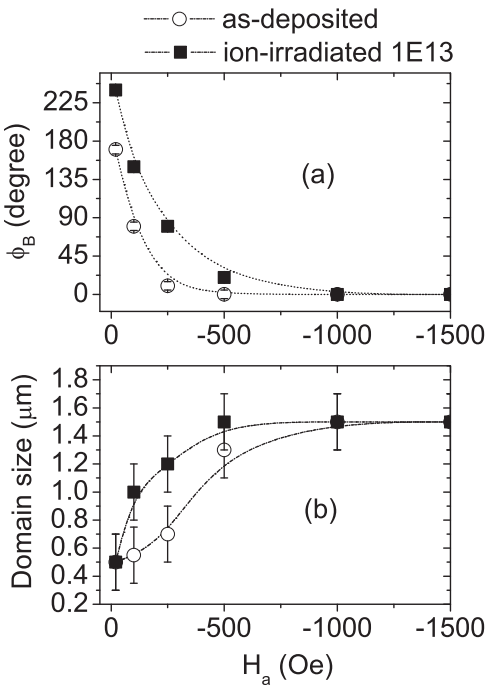

Figure 9. (a) Mean magnetization angle ϕ_B between the nth and the $(n+1)$th layer for the as-deposited and ion-beam-irradiated specimens as obtained from the fits to the NSF reflectivities. (b) Variation in domain size with field as obtained from the simulation of the SF diffuse spectra along Q_x.

3.2.4. Domain size variation. The domain size ξ variation along Q_x ($\xi_\parallel$), as obtained from the simulation of the diffuse scattering SF spectra, is plotted in figure 9(b). In our model, the mean magnetization w.r.t. the applied field varies from region to region around a mean angle ϕ_n with a Gaussian distribution of width $\Delta\phi_n$. In this model, both the components of magnetization parallel (along the y-axis) and perpendicular (along the x-axis) to H_a will contribute to the diffuse scattering signal. The Fourier transform of the pair correlation functions for transverse as well as longitudinal fluctuations (averaging over the surface of the coherence regime and integrating along the unresolved y-axis) within a laterally homogeneous length scale of $2\xi_{(x,y)}$ can be expressed as functions of Lorentzian shapes,

$$\langle F(Q_{x,y}) \cdot F^*(Q_{x',y'})\rangle \approx \mathcal{C}(xx', yy') \cdot \left[\frac{\xi(x, y)}{1+(Q\cdot\xi(x, y))^2} + \frac{\xi(x', y')}{1+(Q\cdot\xi(x', y'))^2}\right], \tag{1}$$

where $\mathcal{C}(xx', yy')$ are the respective amplitudes of fluctuations parallel and perpendicular to the quantization axis. Here, F is the Fourier transform of the perturbed potential $V_{\text{perturbed}}(x, y, z)$, which can be written as

$$V_{\text{perturbed}}(x, y, z) = \frac{2\pi\hbar^2}{m}(\rho_n \pm \rho_m), \tag{2}$$

where ρ_n and ρ_m denote the respective nuclear and magnetic lateral scattering-length density fluctuations within the DWBA.

The lateral correlation of in-plane magnetization is seen to vary from 0.5 μm at 20 Oe to $\sim$1.5 μm at about 1.5 kOe for as-deposited and for the ion-beam-irradiated specimen. However,

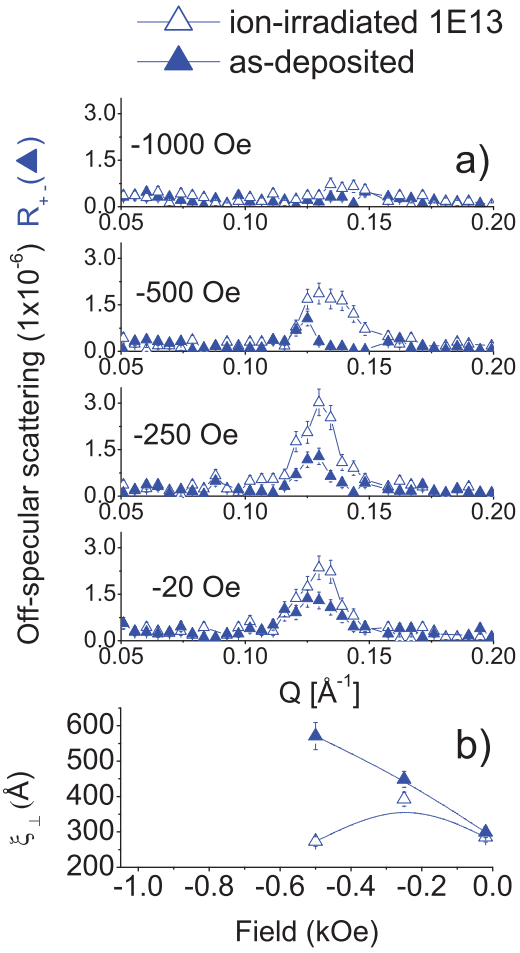

Figure 10. (a) Experimental SF intensity (I_{+-}) of an SiO_2/Co(1.45 nm)/[Cu(1.02 nm)/Co(1.45 nm)]$_{N=20}$ ML at different H_a values. (b) Variation in vertical correlation length with field as obtained from the SF diffuse scattering signal along Q_z.

the variation is somewhat different as larger vertically correlated domains are seen to be formed much earlier after ion irradiation than the as-deposited sample. One can probably correlate this increase in domain size with the loss of uniaxial anisotropy that has been observed from MOKE. One may recall that the MOKE curves along the hard-axis and the easy-axis were quite similar upon an irradiation fluence of 1E13 ions cm^{-2}. As the neutron measurements are performed along the hard-axis of the samples, the readiness in attaining saturation can therefore be understood.

An interesting feature that one further notices is a change in the domain size variation along Q_z ($\xi_\perp$). Looking at the diffuse intensity maps alone may or may not reveal the changes in longitudinal correlation. Such a variation is, however, explicit as we plot the diffusely scattered intensities along Q_z in figure 10(a). The relaxation of vertical correlation upon ion irradiation is most prominent around 500 Oe. A full-width at half-maximum (FWHM) of the peaks is plotted for various fields in figure 10(b). For the as-deposited specimen, $\xi_\perp$ is extended through the entire stack of the ML ($\approx$500 Å). This correlation is significantly reduced to $\approx$300 Å when the specimen is ion irradiated.

3.2.5. S_e values and track radius. It is interesting to note that low-energy ions may contribute to interlayer coupling modifications via phonon annealing similar to gentle thermal annealing effects [10]. A similar mechanism is also true for high-energy ions. In the present case, the energy is partially dissipated in the lattice via electron–phonon (E–P) interaction. The deposited energy is shared between the target electrons and the lattice atoms via electron–electron and E–P interactions, respectively. In such cases, numerical calculations are generally employed to quantify the effects of the interactions using two coupled differential equations. A reasonable correspondence can be found in the case of fs laser pulses, which is supported by experiments as well [6]. Considering the lattice temperature to be not much smaller than the Debye temperature, the E–P coupling factor g is given by

$$g = \frac{\pi^2 m_e n_e v^2}{6\tau_e(T_e)T_e}, \tag{3}$$

where $\tau_e(T_e)$ is the electron mean free time at temperature T_e (which can be related to the Lorentz number and electrical conductivity), v is the speed of sound in metal, m_e is the electron mass and n_e (= valence electron number × atomic density) is the electron number density. The value calculated is linked to an approximate estimation (30% uncertainties of input parameters) of S_e via the delta-ray theory of radial energy distribution. The number of created defects can be determined by measuring *in situ* the resistivity increment as a function of the ion fluence and the time of irradiation.

A swift heavy ion interacts mainly with valence and core electrons, producing energetic electrons. The excited electrons lose energy to the lattice through electron–ion interactions, resulting in a cooling of the electrons and an increase in the lattice temperature. The electrons are therefore effectively in equilibrium with the lattice, at least locally, with roughly equal electronic and lattice temperatures. In the framework of the thermal spike model, Seitz and Koehler [30] predicted that the lattice temperature in the core of an ion track can reach 500 K in noble metals, whereas in transition metals the core temperature may reach up to 5×10^4 K. The maximum electronic temperature that the system could reach, as a function of the electronic energy loss dE/dx and for different initial energy depositions, has recently been calculated by Caron *et al* [31] as well. The range of temperatures are indicative of the same order. In determinations using fs laser irradiation [32], the E–P coupling factor (g) is found to be about 1.25×10^{11} J K^{-1} cm^{-3} s^{-1} for Cu at room temperature and even higher for Co ($g = 34.5 \times 10^{11}$ J K^{-1} cm^{-3} s^{-1} taking the number of valence electron as 2). The temperature of the electronic system increases during a time equivalent to the deposition time ($\sim 10^{-15}$ s). The lattice temperature increases due to the E–P interaction. This leads to a temperature increase of the order of 5×10^4 K within a range of 10 nm (molten phase) along the ion path [6]. The temperature increase is then followed by a rapid quenching (10^{14} K s^{-1}) that results in a latent track structure when the melt solidifies.

However, it is difficult to produce latent tracks in the metallic target as the large number of mobile conduction electrons present in the target screen the space charge created. Nevertheless, they can be created only when the amount of electronic energy loss is higher than the corresponding threshold value of a few keV nm^{-1}. For our system (which can be approximated as $Co_{0.5}Cu_{0.5}$), the $S_e = dE/dx$ is greater than 35 keV nm^{-1} (TRIM), which can give the latent track radius of about ≈ 2–10 nm. The radius of track formation has been shown to be almost a linear function of the electronic stopping power within a certain range of S_e values [33]. Further, the experimental track radius (a few nm) for Co has been shown to be similar to the theoretical

calculation in the case of 5–20 MeV U ions [6]. The threshold of defect creation S_e values calculated for such ion energies is about 28–34 keV nm^{-1}. Now, if we follow our figure 2(a), we can see that for our Co–Cu system, a similar S_e value is not achievable below 125 MeV of Ag ions. It may also be noted that the S_e values have a saturating tendency beyond 150 MeV. In the case of a lower-energy Ag ion ($\leqslant$100 MeV), we would have been within a range of increasing S_e value. Thus, a nanometric scale track radius is conjectured for our 200 MeV Ag ions. Arguably, a saturated S_e value is also possible to achieve using another ion (e.g. Si), as shown in figure 2(b). However, a lower S_e value (10 keV nm^{-1}) would have resulted in a much reduced track radius (<1 nm). Such a track radius would not have caused any observable magnetic variations.

A few other examples show a similar range of track radii for other materials as well. The electron microscopic image of SiO_2 quartz shows a 5.5 nm track radius upon 0.3 MeV of Pb ions [33]. A latent track created in fused silica by a 200 MeV Ag beam (the same energy of the same ion used in the present case) is also about 6.0 nm [34]. The growth of Au nanoparticles ($\sim$10.0 nm) under swift heavy ion irradiation can be achieved by irradiation with 90 MeV Ni [35]. Recently, it was shown that equally spaced dots, each separated by a few tens of nanometers, can be created by single high-energy ($\sim$1 MeV) Xe ion on $SrTiO_3$ crystal [36]. As mentioned before, high-energy ion tracks are straighter and more focused than the low-energy ion tracks that are distributed [12]. This makes them more susceptible to form local variations within a few nanometers of the target layer as compared to that due to low-energy ions.

Materials with strong E–P coupling are sensitive to electronic energy loss, suggesting that the thermal spike is an ingredient in the damage process. Noble metals such as Ag and Cu with a weak E–P coupling are insensitive to S_e, whereas S_e induced defects are created in Ti, Co and Fe as they exhibit stronger E–P coupling. The calculated threshold of defect creation induced by S_e for Co is about 28–34 keV nm^{-1} for 5–20 MeV ions [6]. Our TRIM calculation also indicates very similar S_e values with 200 MeV Ag ions. Thus the system may be within the range of radiation damage. However, due to positive heat of mixing for Co and Cu, no interdiffusion takes place at the interfaces. This does not exclude any local nano-metric scale modification of magnetization. Local heat (current or laser)-induced magnetization modification affecting the local coercive field (without an external field) is not uncommon in thin films [37]. Latent tracks have been observed to drastically modify the magnetic properties in Fe/Si multilayers as an example of the electronic-energy-deposition-induced effects in metallic materials by MeV ions [38].

The physical processes governing the magnetization at a local level are complicated and should involve electron, phonon and spin interactions. The electron temperature rapidly increases up to and often above the Curie temperature, required for demagnetization. The rate of energy transfer from the conduction electrons takes place with a characteristic relaxation time determined by the coupling between the conduction electrons and the spins. This is followed by a recovery of the micromagnetic exchange after the passage of the ions.

A problem associated with the programming of MRAM (magnetic random access memory) is that the required current is orders of magnitude higher than that needed for many other memory devices (SRAMs or DRAMs). One can tackle this problem by providing local heat sources (which do not affect the structure) in close proximity to the memory elements so that one can lower the threshold of magnetization while programming. Swift heavy ions can cause such local heating (with a radius of a few nanometers) that can be realized through the entire stack of the multilayer.

4. Conclusions

We have used the microscopic depth-sensitive technique of polarized neutron scattering to show the effect of swift heavy ions within an antiferromagnetically coupled system. The system shows neither drastic structural or interfacial modifications nor significant macroscopic magnetic property changes, such as magnetoresistance. What makes the study interesting and significant is that it shows the capability of the ions to modify the magnetic structure locally at a nanometric level. Such a local nanometric scale variation may not affect the macroscopic properties but can result in changes of the magnetic coupling behavior or magnetic anisotropy energy due to a change in the magnetic correlations (in-plane and out-of-plane). Such local access to the magnetization can perhaps be used for programming memory elements, even at depths.

Acknowledgments

The authors are thankful to Dr D K Avasthi for providing access to the ion-irradiation facility at the Nuclear Science Center, New Delhi.

Author contributions: AP and SM made the measurements and AP planned the project, prepared the sample, analyzed the data and wrote the manuscript.

References

[1] Johnson W L, Cheng Y T, Van Rossum M and Nicolet M-A 1985 *Nucl. Instrum. Methods* B **7/S** 657
[2] Cheng Y T 1987 *PhD Thesis* California Institute of Technology
[3] Rossi F and Natasi M 1981 *J. Appl. Phys.* **69** 1310
[4] Myers S M 1980 *Nucl. Instrum. Methods* B **168** 265
[5] Dunlop A and Lesueur D 1993 *Radiat. Eff. Defects Solids* **126** 123
[6] Wang Z G, Dufour Ch, Paumier E and Toulemonde M 1994 *J. Phys.: Condens. Matter* **6** 6733
Wang Z G, Dufour Ch, Paumier E and Toulemonde M 1995 *J. Phys.: Condens. Matter* **7** 2525
[7] Dhar S, Schaaf P, Bibic N, Hooker E, Milosavljevic M and Lieb K P 2003 *Appl. Phys.* A **76** 773780
[8] Chappert C, Bernas H, Ferre J, Kottler V, Jamet J-P, Chen Y, Cambril E, Devolder T, Rousseaux F, Mathet V and Launois H 1998 *Science* **280** 1919
[9] Fassbender J, Ravelosona D and Samson Y 2004 *J. Phys. D: Appl. Phys.* **37** R179
[10] Demokritov S O, Bayer C, Poppe S, Rickart M, Fassbender J, Hillebrands B, Kholin D I, Kreines N M and Liedke O M 2003 *Phys. Rev. Lett.* **90** 097201
[11] Mougin A, Mewes T, Jung M, Engel D, Ehresmann A, Schmoranzer H, Fassbender J and Hillebrands B 2001 *Phys. Rev.* B **63** 060409
[12] Avasthi D K and Pivin J C 2010 *Curr. Sci.* **98** 780
[13] Paul A, Gupta A, Chaudhari S M, Phase D M, Ghosh S and Avasthi D K 1999 *Nucl. Instrum. Methods* B **156** 158
[14] Cai M, Veres T, Schiettekatte F, Roorda S and Cochrane R W 2004 *J. Appl. Phys.* **95** 2006
[15] Heinrich B and Bland J A C (ed) 1994 *Ultrathin Magnetic Structures* vol. II (Berlin: Springer)
[16] Wilson I H, Xu J B, Devine R A B and Webb R P 1996 *Nucl. Instrum. Methods* B **118** 473
[17] Marrows C H and Hickey B J 1999 *Phys. Rev.* B **59** 463
[18] Paul A and Lodha G S 2002 *Phys. Rev.* B **65** 245416
[19] Salditt T, Metzger T H and Peisl J 1994 *Phys. Rev. Lett.* **73** 2228
[20] Savage D E, Kleiner J, Schimke N, Phang Y H, Jankowski T, Jacobs J, Kariotis R and Lagally M G 1991 *J. Appl. Phys.* **69** 1411

[21] Paul A, Buchmeir M, Bürgler D E, Rücker U and Schneider C M 2008 *Phys. Rev.* B **77** 224410
[22] Toperverg B P 2002 *Polarized Neutron Scattering* (*Matter and Materials* vol. 12) (Jülich: Forschungszentrum Jülich)
[23] Anker J F and Felcher G P 1999 *J. Magn. Magn. Mater.* **200** 741
[24] Nevot L and Croce P 1980 *Revue Phys. Appl.* **15** 761
[25] Paul A, Damm T, Bürgler D E, Stein S, Kohlstedt H and Grünberg P 2003 *J. Phys.: Condens. Matter* **15** 2471
[26] Neubauer M, Lieb K P, Schaaf P and Uhrmacher M 1996 *Phys. Rev.* B **53** 10237
[27] Grünberg P, Schreiber R, Pang Y, Brodsky M B and Sowers H 1986 *Phys. Rev. Lett.* **57** 2442
[28] Schad R, Beliën P, Verbanck G, Moshchalkov V V, Bruynseraede Y, Fischer H E, Lefebvre S and Bessiere M 1999 *Phys. Rev.* B **59** 1242
[29] Paul A, Kentzinger E, Rücker U, Bürgler D E and Brückel Th 2006 *Phys. Rev.* B **73** 094441
[30] Seitz F and Koehler J S 1956 *Solid State Physics* ed F Seitz and D Turnbull (New York: Academic) vol. 2 p305
[31] Caron M, Rothard H, Toulemonde M, Gervais B and Beuve M 2006 *Nucl. Instrum. Methods Phys. Res.* B **245** 36
[32] Brorson S D, Kazeroonian A, Moodera J S, Face D W, Cheng T K, Ippen E P, Dresselhaus M S and Dresselhaus G 1990 *Phys. Rev. Lett.* **64** 2172
Toulemonde M, Paumier E and Dufour C 1993 *Radiat. Eff. Defects Solids* **126** 201
[33] Meftah A, Brisard F, Costantini J M, Dooryhee E, Hage-Ali M, Hervieu M, Stoquert J P, Studer F and Toulemonde M 1994 *Phys. Rev.* B **49** 12457
[34] Mohanty T, Satyam P V, Mishra N C and Kanjilal D 2003 *Radiat. Meas.* **36** 137
[35] Mishra Y K, Avasthi D K, Kulriya P K, Singh F, Kabiraj D, Tripathi A, Pivin J C, Bayer I S and Biswas A 2007 *Appl. Phys. Lett.* **90** 073110
[36] Akcltekin E, Peters T, Meyer R, Duvenbeck A, Klusmann M, Monnet I, Lebius H and Schleberger M 2007 *Nat. Nanotechnol.* **2** 290
[37] Onoue T, Siekman M H, Abelmann L and Lodder J C 2005 *J. Magn. Magn. Mater.* **287** 501
[38] Dufour C, Bauer Ph, Marchal G, Grilhe J, Jaouen C, Pacaud J and Jousset J C 1993 *Europhys. Lett.* **21** 671